

**Repository of the Max Delbrück Center for Molecular Medicine (MDC)
in the Helmholtz Association**

<https://edoc.mdc-berlin.de/17728>

**On the relation between filament density, force generation and
protrusion rate in mesenchymal cell motility**

Dolati, S., Kage, F., Mueller, J., Müsken, M., Kirchner, M., Dittmar, G., Sixt, M., Rottner, K., Falcke, M.

This is a copy of the final article, which was originally published in:

Molecular Biology of the Cell
2018 NOV 01 ; 29(22): 2674-2686
doi: [10.1091/mbc.E18-02-0082](https://doi.org/10.1091/mbc.E18-02-0082)

Publisher: [The American Society for Cell Biology \(ASCB\)](http://www.ascb.org)

This article was originally distributed by The American Society for Cell Biology under license from the author(s). Two months after publication it is available to the public under the following license:



Copyright © 2018, Dolati et al. This work is licensed under a Creative Commons Attribution-NonCommercial-ShareAlike 3.0 Unported license, as described at <http://creativecommons.org/licenses/by-nc-sa/3.0/>. To view a copy of this license, visit <http://creativecommons.org/licenses/by-nc-sa/3.0/> or send a letter to Creative Commons, PO Box 1866, Mountain View, CA 94042, USA.

On the relation between filament density, force generation, and protrusion rate in mesenchymal cell motility

Setareh Dolati^a, Frieda Kage^{b,c}, Jan Mueller^d, Mathias Müsken^e, Marieluise Kirchner^a, Gunnar Dittmar^f, Michael Sixt^d, Klemens Rottner^{b,c,*}, and Martin Falcke^{a,g,*}

^aMax Delbrück Center for Molecular Medicine, 13125 Berlin, Germany; ^bDivision of Molecular Cell Biology, Zoological Institute, Technische Universität Braunschweig, 38106 Braunschweig, Germany; ^cDepartment of Cell Biology and ^eCentral Facility for Microscopy, Helmholtz Centre for Infection Research, 38124 Braunschweig, Germany; ^dInstitute of Science and Technology Austria, 3400 Klosterneuburg, Austria; ^fDepartment of Oncology, Luxembourg Institute of Health, L-1445 Strassen, Luxembourg; ^gDepartment of Physics, Humboldt Universität, 12489 Berlin, Germany

ABSTRACT Lamellipodia are flat membrane protrusions formed during mesenchymal motion. Polymerization at the leading edge assembles the actin filament network and generates protrusion force. How this force is supported by the network and how the assembly rate is shared between protrusion and network retrograde flow determines the protrusion rate. We use mathematical modeling to understand experiments changing the F-actin density in lamellipodia of B16-F1 melanoma cells by modulation of Arp2/3 complex activity or knockout of the formins FMNL2 and FMNL3. Cells respond to a reduction of density with a decrease of protrusion velocity, an increase in the ratio of force to filament number, but constant network assembly rate. The relation between protrusion force and tension gradient in the F-actin network and the density dependency of friction, elasticity, and viscosity of the network explain the experimental observations. The formins act as filament nucleators and elongators with differential rates. Modulation of their activity suggests an effect on network assembly rate. Contrary to these expectations, the effect of changes in elongator composition is much weaker than the consequences of the density change. We conclude that the force acting on the leading edge membrane is the force required to drive F-actin network retrograde flow.

Monitoring Editor

Laurent Blanchoin
CEA Grenoble

Received: Feb 2, 2018

Revised: Aug 20, 2018

Accepted: Aug 22, 2018

INTRODUCTION

Lamellipodia are flat, actin-rich cell surface structures mediating efficient protrusion and migration on planar substrates in various cell types and conditions (Small *et al.*, 2002; Pollard and Borisy, 2003; Rottner *et al.*, 2017). It is commonly agreed that these structures

comprise networks of actin filaments that are initiated and maintained by the continuous activity of the actin-related protein 2/3 (Arp2/3) complex (Suraneni *et al.*, 2012; Wu *et al.*, 2012; Koestler *et al.*, 2013) mediating branching of daughter filaments off mother filaments (Mullins *et al.*, 1998; Pollard and Borisy, 2003). The Arp2/3 complex is activated by its lamellipodial activator WAVE regulatory complex (WRC). Branch formation is followed by separation of WRC from the Arp2/3 complex, with the latter being incorporated into the network and the former remaining at the membrane for additional cycles of Arp2/3 complex activation (Pollard and Borisy, 2003; Iwasa and Mullins, 2007; Lai *et al.*, 2008). Protrusion of lamellipodial actin networks is driven by polymerization of the filaments abutting the membrane (Small and Resch, 2005; Mueller *et al.*, 2017). The fast-growing, barbed filament ends continue to grow until capped, with the growth aided by elongation factors residing at their tips (Mejillano *et al.*, 2004; Pollard and Cooper, 2009; Shekhar *et al.*, 2016).

Although Arp2/3 complex activation by the WRC is essential for the formation of these structures (Machesky and Insall, 1998;

This article was published online ahead of print in MBoC in Press (<http://www.molbiolcell.org/cgi/doi/10.1091/mbc.E18-02-0082>) on August 29, 2018.

*Address correspondence to: Martin Falcke (martin.falcke@mdc-berlin.de) or Klemens Rottner (k.rottner@tu-braunschweig.de).

Abbreviations used: ABP-280, actin-binding protein 280; Arp2/3, actin-related protein 2/3; EGFP, enhanced green fluorescent protein; Ena/VASP, enabled/vasodilator-stimulated phosphoprotein; ER, elastic region; F-actin, filamentous actin; FMNL, formin-like family member; Nap1, NCK-associated protein 1; Scar/WAVE, suppressor of cAMP receptor/WASP family verprolin-homologous.

© 2018 Dolati *et al.* This article is distributed by The American Society for Cell Biology under license from the author(s). Two months after publication it is available to the public under an Attribution–Noncommercial–Share Alike 3.0 Unported Creative Commons License (<http://creativecommons.org/licenses/by-nc-sa/3.0>).

“ASCB®,” “The American Society for Cell Biology®,” and “Molecular Biology of the Cell®” are registered trademarks of The American Society for Cell Biology.

Steffen *et al.*, 2004; Chen *et al.*, 2010; Rottner *et al.*, 2017), additional factors have recently emerged that generate actin filaments, and significantly contribute to actin network density and protrusion velocity of lamellipodia (Kage *et al.*, 2017). Surprisingly, however, two factors, formin-like family member 2 (FMNL2) and FMNL3, grouping into the formin family of actin assembly factors and accumulating at lamellipodia tips, turned out not to accelerate actin filament networks in lamellipodium protrusion, as previously proposed (Block *et al.*, 2012; Krause and Gautreau, 2014), but instead to generate subpopulations of filaments operating in addition to and thus independently from the Arp2/3 complex-driven network (Kage *et al.*, 2017). Both FMNL2 and 3 contribute to the efficiency of protrusion, but with differential biochemical activities concerning nucleation versus elongation (Kage *et al.*, 2017). The contribution of these activities and of the two formins to lamellipodial protrusion relative to each other and relative to other potential actin polymerases operating at these sites, such as enabled/vasodilator-stimulated phosphoprotein (Ena/VASP) family members (Rottner *et al.*, 1999; Svitkina *et al.*, 2003; Hansen and Mullins, 2015), has remained unknown.

Knocking out or down FMNL2, FMNL3, or both had effects on protrusion velocity and filament density, which elude intuitive mechanistic understanding assuming proportionality between actin assembly rate and protrusion velocity. FMNL2 is the faster elongator (~60% faster than FMNL3 *in vitro*; Kage *et al.*, 2017). The polymerization rate of a single filament depends exponentially on the force on the filament tip (Mogilner and Oster, 2003). Interaction of filaments with different elongators via this force dependency and the leading edge membrane suggests the fastest elongator to contribute the most to protrusion force and velocity. However, knocking down FMNL3 reduced protrusion velocity more (~1.5 fold) than knocking down FMNL2 (Block *et al.*, 2012; Kage *et al.*, 2017). Knocking down both formins by RNA interference (RNAi) reduced the protrusion velocity even further (Kage *et al.*, 2017). CRISPR/Cas9-mediated, simultaneous elimination of FMNL2 and 3 expression reduced protrusion velocities and filamentous actin (F-actin) intensities to roughly 65–70 and 50%, respectively, dependent on KO clone and experiment, whereas lamellipodial F-actin network assembly rates in all clones remained completely unchanged (see Figures 4e and 5, b and d, in Kage *et al.* [2017]). The force exerted by the filament tips on the leading edge membrane drives both protrusion and retrograde flow (Zimmermann *et al.*, 2012). If this force were proportional to the number of filaments per leading edge contour length, we would expect both the protrusion velocity and the retrograde flow velocity to decrease upon FMNL2/3 knockout. Nevertheless, the network assembly rate did not change substantially across all FMNL formin knockout and knockdown experiments, such that protrusion slowed down but retrograde flow sped up by about the same amount (Kage *et al.*, 2017).

Cell motion is overdamped. Velocities are proportional to the driving forces in this regime and the ratios of velocities are equal to the ratios of forces. The ratio of F-actin densities of knockout FMNL2/3 cells to control cells was smaller than the corresponding velocity ratio. Filament numbers decreased relatively more than forces, and hence the ratio of force F per contour length to N ($R_F = F/N$) increased upon formin knockout (Kage *et al.*, 2017).

Robust observations applying to all of the formin knockout/knockdown experiments are a decrease of F-actin density and protrusion velocity, and an increase in R_F while the assembly rate stays constant. Clearly, simple estimates assuming independence of the factors setting the protrusion velocity cannot recapitulate these results. Here we employ mathematical modeling to ask for the

mechanisms explaining these observations and the determinants of protrusion force and velocity as well as network assembly rates.

THE MATHEMATICAL MODEL

We model the protrusion as a cross-linked viscoelastic network of filaments, a concept that has been used and confirmed in several studies (Kruse *et al.*, 2006; Joanny and Prost, 2009; Shemesh *et al.*, 2009; Herant and Dembo, 2010; Barnhart *et al.*, 2011; Shemesh *et al.*, 2012; Camley *et al.*, 2013; Nickaen *et al.*, 2017). Elasticity of the network is due to the elastic properties of filaments and cross-links (Danuser *et al.*, 2013) and has been observed experimentally (Ji *et al.*, 2008; Zimmermann *et al.*, 2012). The viscosity arises from the motion in the cytosol fluid and cross-linker binding and dissociation (Danuser *et al.*, 2013). Consequently, cross-linker concentration also has to be taken into account when determining the mechanical properties of the F-actin network.

We use an auxiliary variable Φ to mark the extension and position of the moving protrusion. That variable is equal to 1 inside the protrusion and 0 outside it. This is a commonly used method for partial differential equations with moving boundaries usually referred to as the phase field method (Shao *et al.*, 2010). The interface between $\Phi = 0$ and $\Phi = 1$ moves with the membrane velocity of the leading edge membrane both at the front and rear. Consequently, the depth of the actin network region modeled by our equations is constant. The equation of motion of the phase field Φ is given in the Supplemental Material. We describe the F-actin network in a thin-film approximation, that is, we average in the direction orthogonal to the substrate, and consider the dynamics along a radial line from the protrusion leading edge toward the cell body. The force balance inside the protrusion is given by the interior force of the network, which is equal to the spatial derivative of the tension σ , and the friction against the cellular components stationary in the lab frame and the membrane (friction coefficient ξ):

$$\frac{\partial(\Phi\sigma)}{\partial x} - \Phi\xi v = 0 \quad (1)$$

The friction force is proportional to the flow velocity v . Friction mediates the interaction of network flow with adhesions and consequently traction forces on the substrate. A corresponding correlation between network flow and traction forces has been observed (Ji *et al.*, 2008; Barnhart *et al.*, 2011).

F-actin network flow is rearward at the front. It moves with the forward cell velocity at the rear of the cell. Hence, there is a range in some distance from the leading edge membrane where the network velocity is equal or very close to 0. This is where we place the rear end of our simulation area. Tension and velocity vanish at this point, that is,

$$\left. \frac{\partial\sigma}{\partial x} \right|_{x=0} = \sigma(x=0) = 0 \quad (2)$$

The force exerted by polymerizing filaments against the leading edge membrane determines the tension at the front $x = L$.

We describe the viscoelastic properties of the cross-linked F-actin network by the advected Maxwell model as suggested by the seminal work by Kruse *et al.* (2005, 2006):

$$2\eta \frac{\partial}{\partial x} (\Phi v) = \left[1 + \tau \frac{\partial}{\partial t} + \tau v \frac{\partial}{\partial x} \right] \Phi \sigma \quad (3)$$

In Eq. 3, τ is the relaxation time of the gel. It is set by the ratio of viscosity η and elastic modulus E ($\tau = \eta/E$). These properties depend on the network volume density and the degree of cross-linking in the filament network.

Retrograde flow necessarily entails a gradient of free cross-linkers C , which may lead also to a gradient of bound ones B (Falcke, 2016). Bound cross-linkers are advected with the retrograde flow and dissociate (rate constant k^-) on their way back or are set free when the network disassembles. Free cross-linkers diffuse forward toward the leading edge where they cross-link (rate constant k^+) newly polymerized filaments. This is described by a reaction-diffusion equation for C and a reaction-advection equation for B :

$$\frac{\partial(C\Phi)}{\partial t} = D_c \frac{\partial}{\partial x} \left(\Phi \frac{\partial C}{\partial x} \right) - k^+(B_T - B)C\Phi + k^- B\Phi \quad (4)$$

$$\frac{\partial(B\Phi)}{\partial t} = -\frac{\partial}{\partial x} (v B\Phi) + k^+(B_T - B)C\Phi - k^- B\Phi \quad (5)$$

B_T is the total concentration of available cross-linker binding sites on the network. We assume B_T to equal one-third of F-actin monomers. The bulk concentration in the cell body determines one boundary condition $C(x=0) = C_{\text{bulk}}$. No flux boundary conditions $\partial C / \partial x = 0$ apply at the front for free cross-linkers. Newly polymerized filaments are not cross-linked yet, which entails $B = 0$ at the front. Arp2/3 complex-mediated branching occurs at the leading edge and could be perceived as a new type of filament link changing elastic properties of the F-actin network. However, detailed calculations revealed that as opposed to the X structure of cross-links, the Y structure of branches does not change elastic properties substantially (Razbin *et al.*, 2015), because the mother filament alone essentially carries all the load. Details about the implementation of boundary conditions can be found in the Supplemental Material.

The cross-linking dynamics may create a depletion zone of cross-linkers close to the membrane (Falcke, 2016), where filaments are not linked due to lack of free cross-linkers. We call that range the elastic region (ER). Studies with F-actin solutions showed rather coherently that network elastic moduli are not affected by the presence of cross-linkers below a critical molecule number ratio cross-linkers/actin of ~3% (Janmey *et al.*, 1994; Nakamura *et al.*, 2002; Gardel *et al.*, 2004). The depth z of the ER is the distance from the leading edge where the cross-linker concentration reaches this critical value. The dynamics of the ER depth is determined by the velocity V_{link} of this concentration level and the protrusion velocity.

The mean contour length l of filaments in the ER grows with the polymerization rate V_P and decreases due to cross-linking:

$$\dot{l} = V_P - \max \left(1, \frac{l}{z} \right) V_{\text{link}} \quad (6)$$

The factor of V_{link} accounts for the bending of filaments in the ER such that motion cross-links more filament contour length than the distance traveled in lab space.

The polymerization of actin filaments that generates the driving force occurs in the ER at the leading edge membrane. It is catalyzed by actin filament elongators. We describe it as a two-step process: binding of an actin monomer to the complex with rate k' , and elongation, the rate of which depends exponentially on the product of single filament force f and filament length d added by one monomer $ke^{-fd/k_b T}$. Dissociation of an actin monomer from the complex before elongation is assumed to be negligible. The total time for the addition of one monomer is $1/k' + d/ke^{-fd/k_b T}$. The polymerization rate is the inverse of this time, times d :

$$V_P = \frac{d k' ke^{-fd/k_b T}}{d k' + ke^{-fd/k_b T}} \quad (7)$$

The polymerization rate increases and then saturates with increasing pulling force as suggested by data in Kozlov and Bershadsky (2004), Courtemanche *et al.* (2013), and Jégou *et al.* (2013). Please see Kozlov and Bershadsky (2004) and Shemesh and Kozlov (2007) for more detailed models of processive elongation by formins.

We calculate the force exerted by a single filament on the membrane using the worm-like chain model (Kroy and Frey, 1996):

$$f(l, z) = k_{\parallel}(z - R_{\parallel}(l)) \quad (8)$$

Here k_{\parallel} is the mean spring constant of filaments averaged over the angular distribution of filaments (calculations in the Supplemental Material). The spring constant for a single filament is proportional to l^{-4} (Kroy and Frey, 1996), hence, the network structure, force, and polymerization rate are coupled. The experiments on modulation of cross-linker properties in fibroblasts by Ehrlicher *et al.* (2015) are consistent with this view. The equilibrium length R_{\parallel} of the filament obeys $R_{\parallel}(l) = l(1 - l/2l_p)$, in which l_p is the persistence length of the filament. We describe the mechanical properties of the ER as the sum of the properties of the individual filaments. Consequently, the total force F per leading edge contour length is $F = Nf$, with N being the number of filaments per leading edge contour length.

Calculated elasticity of the ER couples with the elastic modulus of the viscoelastic gel and follows the concentration profile of bound cross-linkers to a maximum bulk elasticity of the network. The bulk elasticity and the viscosity of the gel depend on the volume density of filaments (see Supplemental Material Section 4).

All the parameters used in the model are listed in Supplemental Tables S1–S3. In the Supplemental Material, we investigate the effect of variation of parameters on the behavior of the system, for which we do not have precise experimental measurements (Supplemental Figures S1 and S2).

RESULTS

Before going into simulation results, and to confirm the correlation of F-actin density and protrusion rate, we sought to reduce the amounts of actin filaments present in lamellipodia by means other than deleting FMNL formin function. We experimentally interfered with Arp2/3 complex function specifically in lamellipodia, but not other subcellular regions, and in controlled, average cell populations. This was achieved through CRISPR/Cas9-mediated disruption of the gene encoding NCK-associated protein 1 (Nap1), also termed Nckap1, one of five subunits of the ubiquitously expressed WRC, which is considered essential for connecting Rac signaling to Arp2/3 complex activation in lamellipodia (Kunda *et al.*, 2003; Steffen *et al.*, 2004, 2013). However, Nap1 KO was, to our surprise, partially compensated by expression of the mostly hematopoietic Nap1 orthologue NCK-associated protein 1 like (Nckap1l), also known as Hem1 (Leithner *et al.*, 2016).

Two distinct Nap1 KO clones were selected, which formed lamellipodia with a frequency (cells with lamellipodia on laminin) of 15% (KO #6) and 70% (KO #21), with the latter constituting the best performing clone isolated (frequency of lamellipodia formation of B16-F1 WT cells: 85%). These differential activities were concluded to derive from variable, compensatory Hem1 expression and thus remaining protein levels of the WRC subunit and lamellipodial Arp2/3 complex activator suppressor of cAMP receptor/WASP family verprolin-homologous (Scar/WAVE) (Rottner *et al.*, 2017), with Nap1 KO #21 displaying highest Hem1 expression among Nap1 null clones (*Materials and Methods* and unpublished data). We thus figured that Nap1 null clones displaying differential Hem1

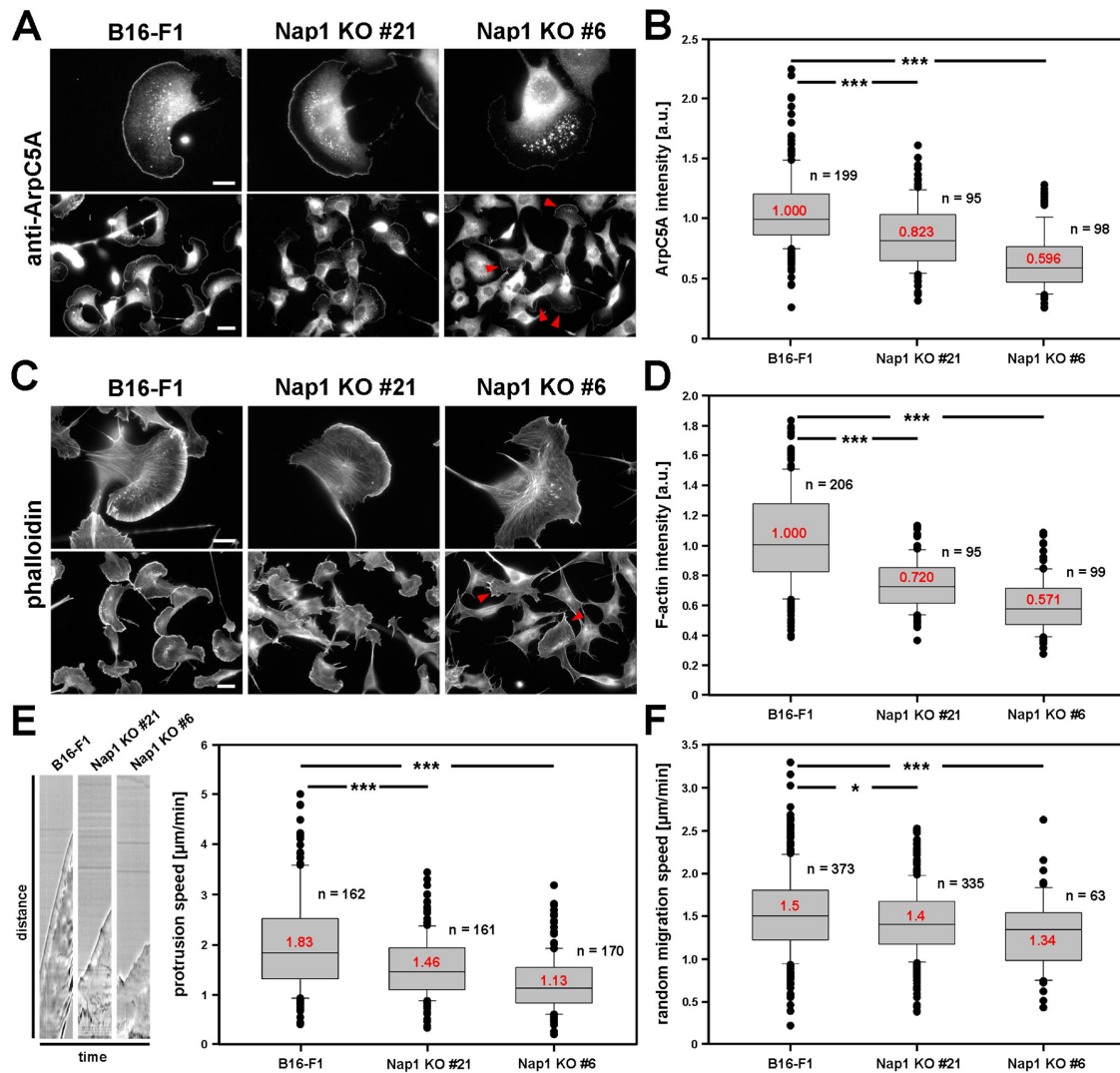


FIGURE 1: Arp2/3 complex activity in lamellipodia correlates with F-actin intensity and protrusion as well as migration rates. B16-F1 WT and two selected Nap1 null clones expressing differential Hem1 levels (#21 high and #6 low) were subjected to analysis of lamellipodial parameters, as indicated. (A) Representative high magnification (top) and overview images (bottom) of respective cells stained for Arp2/3 complex (ArpC5A). (B) Quantifications of Arp2/3 complex intensities in respective clones. Note the significantly reduced frequency of lamellipodia formation and the intensity of lamellipodial Arp2/3 complex staining in Nap1 KO #6 (red arrowheads in A), as confirmed by the intensity quantifications in B. (C, D) Differential intensities of lamellipodial actin filaments (phalloidin staining) in respective clones, as indicated. Bars in the top panels of A and C correspond to 10 μm , and in the bottom panels to 20 μm . Lamellipodial actin filament levels are reduced by 28% (KO #21) and 43% (KO #6). For illustration of the method of determining lamellipodial F-actin and Arp2/3 complex intensities, see Supplemental Figure S10. (E, F) Analysis of lamellipodial protrusion speed and random cell migration in respective clones. Left part in E depicts kymographs (space-time plots) of representative cells from control and the two distinct KO clones, exemplifying lamellipodial advancements over time. Note that for all cell populations, only those cells capable of lamellipodia formation were included in analyses. Rates of protrusion upon reduction of Arp2/3 complex incorporation and F-actin intensity are reduced by ~20% (KO #21) and 38% (KO #6). (B, D, E, F) Results from quantifications are displayed as box-and-whiskers plots with median values given in red, boxes including 50% (25–75%) and whiskers 80% (10–90%) of all measurements; outliers are shown as dots. *n*, number of cells analyzed. * corresponds to $p \leq 0.05$ and *** to $p < 0.001$, as determined by nonparametric Mann-Whitney rank sum test.

expression and thus lamellipodial activity can be explored for effects of tuning down WRC activity on lamellipodial protrusion and cell migration rates. We first confirmed that lamellipodial frequency in those clones correlated with changes in the amounts of Arp2/3 complex incorporated into lamellipodia. Interestingly, clone #21 displayed reduced intensities of Arp2/3 complex as compared with B16-F1 wild type, but more Arp2/3 complex in these structures than

the low lamellipodial frequency clone #6 (Figure 1, A and B). These data confirmed that differential lamellipodial frequencies are likely correlated with differential, lamellipodial Arp2/3 complex activities. Strikingly, reduced incorporation of Arp2/3 complex clearly correlated with decreased actin filament intensities in lamellipodia (Figure 1, C and D), again leading to decreased rates of lamellipodial protrusion (Figure 1E), and consequently migration (Figure 1F).

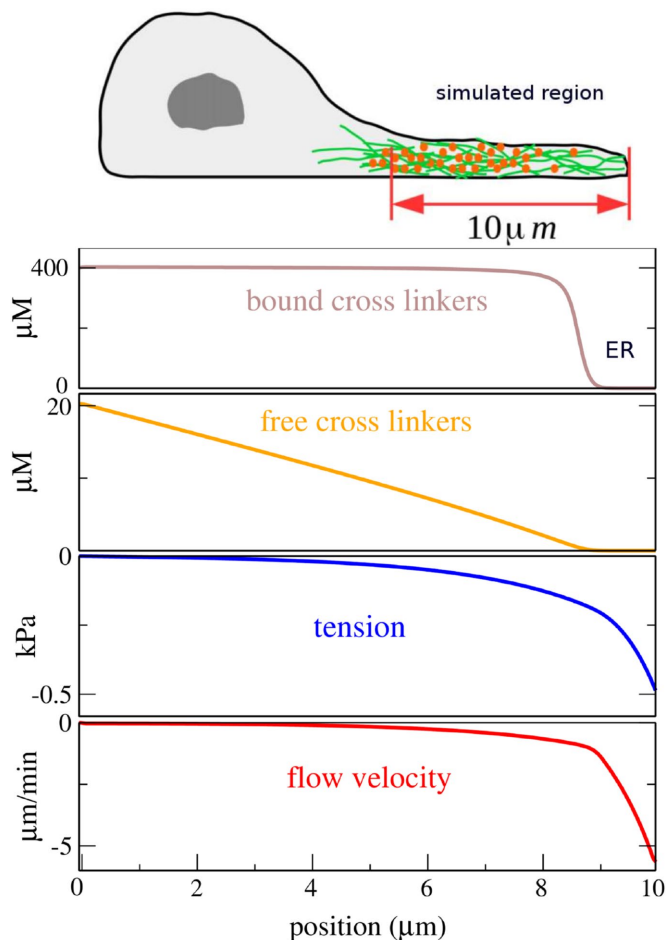


FIGURE 2: Examples of spatial profiles in the radial direction of the steadily moving protrusion as a result of simulating Eqs. 1–6. ER, elastic region with depletion of cross-linkers. The parameter values are in Tables S1–S3 in the Supplemental Material. We always use these values in simulations unless stated otherwise. The sketch at the top indicates the simulated region of the protrusion.

This was clearly reminiscent of the reductions of filament intensities and protrusion as well as migration rates observed in this cell type upon removal of FMNL2 and FMNL3 (Kage *et al.*, 2017).

A typical steady state of concentrations, tension, and velocity profile as a result of simulating Eqs. 1–6 is shown in Figure 2. At the top, we sketch the region of the cell that we simulate. The front is the leading edge membrane in the direction of motion, and the back is ~10 μm deep into the protrusion, where the flow velocity vanishes. The concentration profiles of bound and free cross-linkers illustrate the gradient providing the anterograde diffusive flux of free cross-linkers, and the depletion zone of cross-linkers at the very front. The depth of the ER is ~1 μm in this example. The main function of this region is to account for the coupling between network structure and polymerization rate mentioned in the context of Eq. 8. Such a depletion zone has been observed for actin-binding protein 280 (ABP-280)/filamin and α -actinin in electron micrographs (Svitkina and Borisy, 1999). Its mechanical properties have been confirmed by the force-velocity relation of fish keratocytes (Zimmermann *et al.*, 2012). Note that the boundary of the ER does not necessarily correspond to the zone of lamellipodium-lamella transition, as the lamellipodium is typically broader than the ER.

The tension profile and the retrograde flow velocity exhibit a rapid decay within a few micrometers of the leading edge, and then decay more slowly with increasing distance from the front. This agrees qualitatively with the rapid decay of retrograde flow observed in the lamellipodium rear and the slow flow rates in the lamella in a variety of experiments (Ponti *et al.*, 2004, 2005; Delorme *et al.*, 2007; Koestler *et al.*, 2008; Burnette *et al.*, 2011).

Filament area density, network assembly rate, and protrusion velocity are the observables directly measured. Assembly rate measurements determine the relative velocity between leading edge membrane and the network, that is, the assembly rate is the vectorial difference of the protrusion rate and the average retrograde flow speed (note that the latter one is negative). The measurements averaged retrograde flow velocity over the first few micrometers from the leading edge into the protrusion. We averaged over 3 μm to be compatible with these results in the presentation of simulation results. We choose the number of filaments per leading edge contour length N corresponding to the filament area density as a control parameter in our model. We will change this parameter to mimic formin and Nap1 knockout. Later we will also consider formin sub-type-specific filament subpopulations distinguished by their respective rate of elongation. We start with investigating the effect of changing the filament density with a single population of filaments.

The F-actin intensity in a top down view onto the protrusion measures the filament area density. Given the decrease in area density, the two extreme scenarios for the volume density are the following: 1) The height h of the lamellipodium decreases proportionally to the area density of filaments such that the volume density of filaments stays constant ($h \propto N$). This would entail a change of the tension in the network, that is, the force per protrusion cross-section area driving the network flow, whereas the material properties of the network would not be affected. 2) The height of the lamellipodium stays unchanged and the volume density ρ and area density both decrease to the same extent ($\rho \propto N$). That change in volume density of the network would affect its material properties: elasticity, viscosity, and friction coefficient (MacKintosh *et al.*, 1995; see also Supplemental Material Eqs. S12 and S13).

Scenario 1 is less intuitive and therefore we explain it here in detail (Figure 3). The comparison of two simulations with large and small N illustrates the consequences of the height change for tension and retrograde flow. Tension is higher at the leading edge with a smaller number of filaments than with a large one (Figure 3, A and B). It also decays steeper, and hence flow velocity, which is proportional to the tension gradient (see Eq. 1), is faster with small filament numbers than with large ones. Tension at the front of the network increases with decreasing N (Figure 3C). However, the total force exerted on the leading edge membrane decreases (Figure 3D). The protrusion rate is proportional to the total force and therefore behaves in the same way. It decreases by ~40% when the area density is reduced to 50%. In agreement with experiments, the ratio R_F (the force per leading edge contour length/ N) increases with decreasing N and the network assembly rate changes very little (less than 5%) in the same N range.

Central to the mechanism is that the protrusion velocity is determined by force per leading edge contour length while retrograde flow velocity is set by the tension gradient. Starting from control, a decrease in filament area density entails a decrease in force per leading edge contour length, but an increase in tension due to the reduction in network height.

The results for scenario 2—the change of the material properties of the network—are shown in the Supplemental Material (Supplemental Figure S3). The force per filament exhibits a maximum in its

Scenario 1

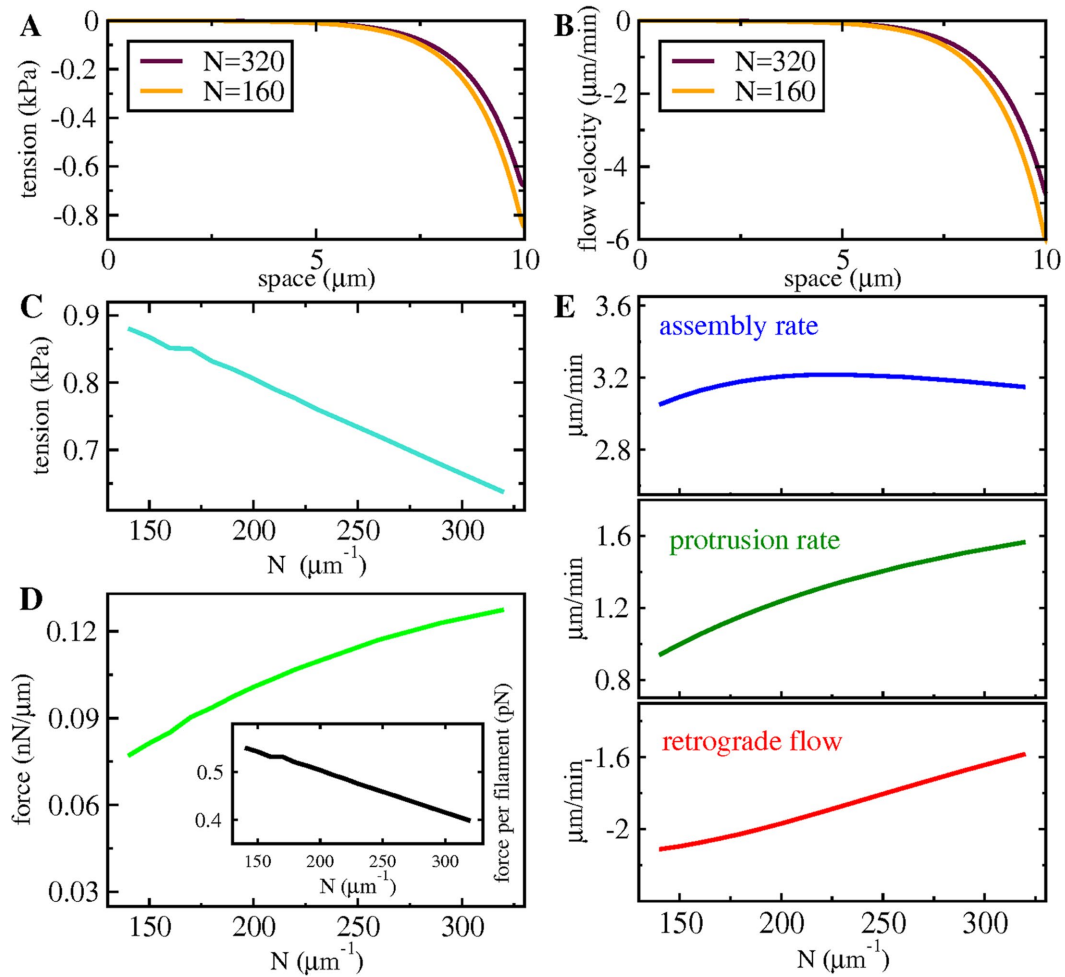


FIGURE 3: Tension, forces, and velocities in scenario 1 ($h \propto N$). (A, B) Tension and velocity profiles with high and low filament density N . (C) The dependency of the tension at the leading edge on filament density N . (D) The dependency of force per leading edge contour length and force per filament on filament density N . (E) The dependency of the network assembly rate, protrusion rate, and retrograde flow on filament density N . The values at large N are in the range of experimental results for control cells (see Kage *et al.*, 2017).

N dependence. The behavior of the retrograde flow and assembly rate change at the value of N with maximal force per filament. Above this N value, the dependence of friction on N dominates the dependence of retrograde flow on N . With low filament density, the protrusion rate decreases by $\sim 45\%$ and the assembly rate drops by $\sim 20\%$ of its control value. With this scenario, the behavior of the assembly rate thus agrees less with the experimental observations than scenario 1.

The tension-based mechanism (scenario 1) produces a behavior very close to the experimental observations upon reduction of filament area density, because the protrusion rate and force per leading edge contour length decrease and the assembly rate stays almost unchanged upon density reduction. However, we do not have experimental evidence for the height h being strictly proportional to N at present (neither do we have data contradicting it). Interestingly, on the basis of estimating lamellipodial heights in different cell lines by structured illumination microscopy (SIM), which can at least increase the resolution in all three dimensions by a factor of 2 as compared with conventional confocal microscopy (Schermelleh *et al.*, 2010), we find an experimentally determinable and statistically

significant reduction of this parameter (Supplemental Figure S4). We note, though, that realistic, absolute numbers for lamellipodial heights or potential changes of height in FMNL2/3 knockout cell lines as compared with controls can admittedly not be derived from this method (see *Materials and Methods* and legend to Supplemental Figure S4). However, an additional hint for a clear correlation between actin network density and lamellipodial height came from side views of electron tomograms of lamellipodia with experimentally induced, transient assembly episodes with low or high actin network density (Mueller *et al.*, 2017). Here, low actin network density clearly correlated with spatially restricted lamellipodial actin network thinning, whereas for high density, the opposite, that is, thickening, was observed (Figure 4). Thus, we assume that h decreases when N decreases. However, h might decrease less than proportional. Therefore, we also investigate the case where the height of the lamellipodium decreases, but less than the area density. We assume an intermediate case between scenario 1 and 2, that is, a 50% decrease in area density entails a 25% decrease in height. The volume density is equal to area density/height and hence decreases accordingly (see Supplemental Material Eq. S16).

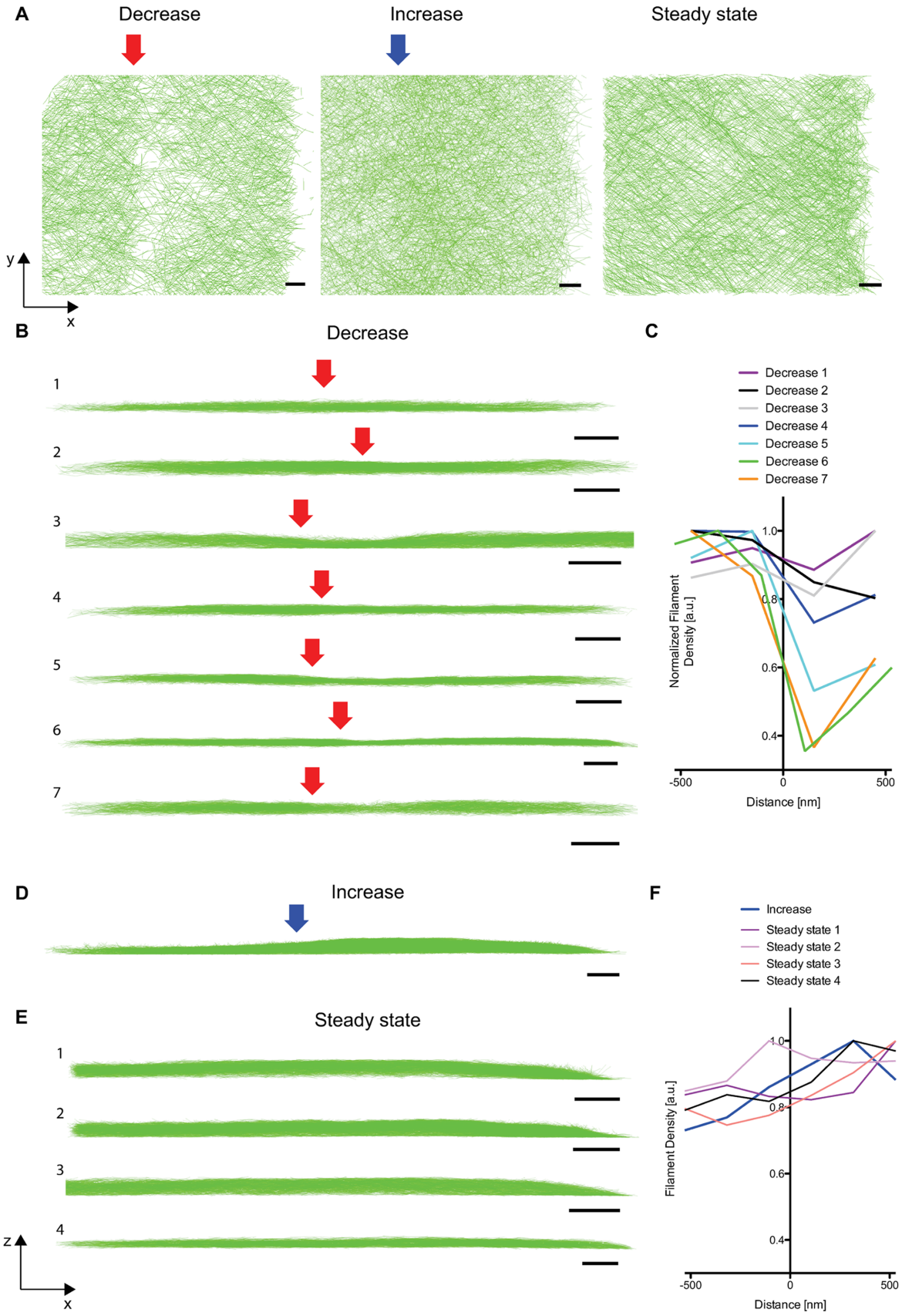


FIGURE 4: Experimentally induced, transient changes of actin network density have an impact on lamellipodial thickness. Side views of correlated electron tomograms show changes in lamellipodial height upon changes in membrane tension. The height change correlates with F-actin density changes. (A) Representative views of electron tomograms of lamellipodia, which were chemically fixed immediately after one of two different

Intermediate scenario

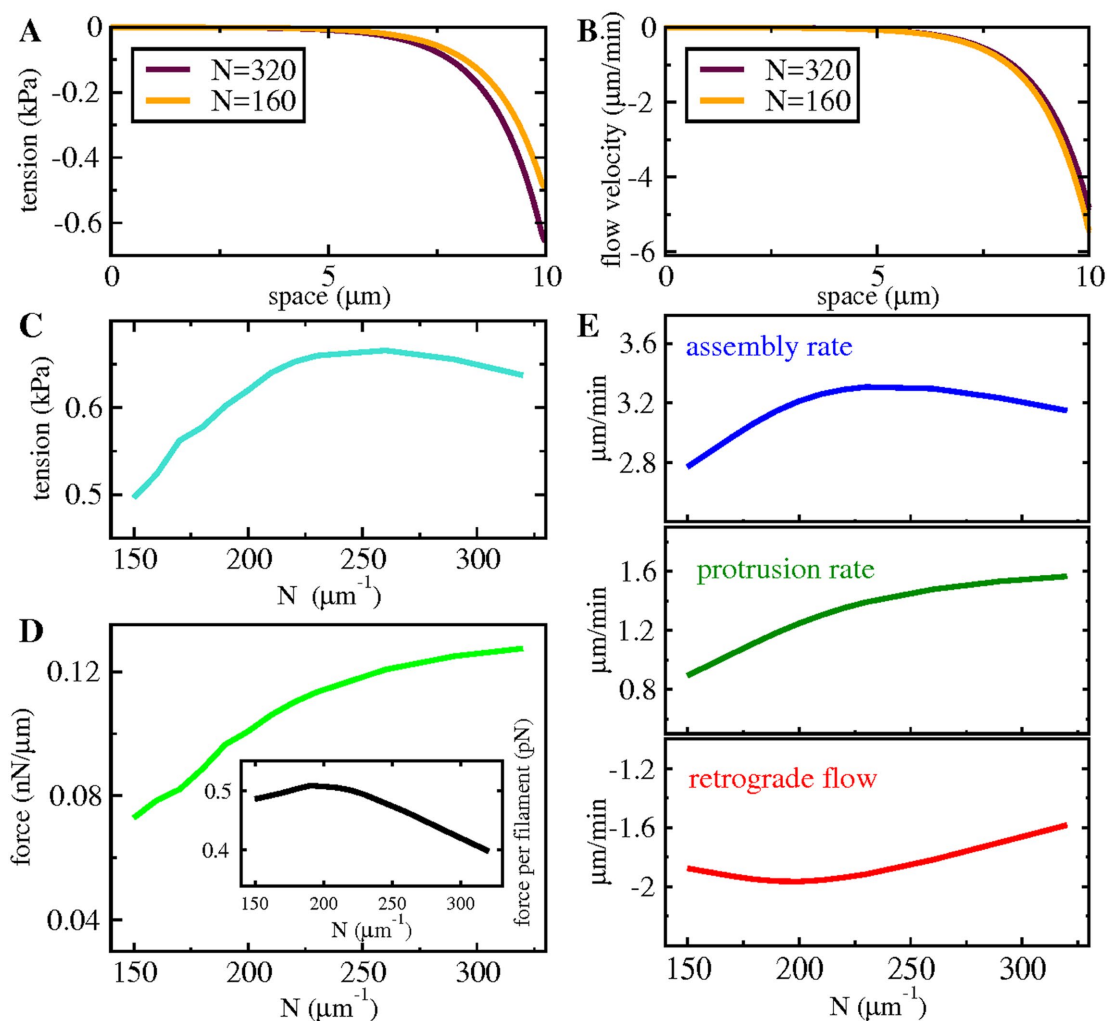


FIGURE 5: Tension, forces, and velocities in the intermediate scenario. (A, B) Tension and velocity profiles with high and low filament density N . (C) The dependency of the tension at the leading edge on filament density N . (D) The dependency of force per leading edge contour length and force per filament on filament density N . (E) The dependency of network assembly rate, protrusion rate, and retrograde flow on filament density N . The values at large N are in the range of experimental results for control cells (Kage *et al.*, 2017). The network assembly rate, which is the vectorial difference of protrusion rate and retrograde flow velocity, first increases very little with decreasing N and then decreases by $\sim 10\%$ compared with control. The protrusion rate is reduced by 45% of its control value at small N values.

Figure 5 shows what the effect of height and tension changes adds to the effect of the material properties in this intermediate case. Down to $\sim 65\%$ of the control value of N , the tension mechanism and the changes in material properties both contribute to

higher retrograde flow and we see an increase in assembly rate when decreasing N . At even smaller N values, the tension also decreases and thus cannot help increasing retrograde flow anymore. The retrograde flow changes its N dependency and the assembly

manipulations: Detachment of part of the cell body to induce a decrease in membrane tension (“Decrease”), with the actin density decrease marked with a red arrow. Microneedle aspiration of the back of the cell body to increase membrane tension (“Increase”), with the actin density increase marked with a blue arrow. As a control, tomograms were acquired at steady state. (B) Side views of the correlated tomograms with an induced decrease in membrane tension and accompanying decrease in filament density marked with red arrows. (C) Actin filament densities before and after experimentally induced tension decrease. The red arrows in B correspond to 0 nm in the graph. Density has been determined as total contour length per area and normalized to the maximum value in the plot. Density is an average over stripes parallel to the leading edge with a breadth of 300 nm. (D) Side view of a correlated tomogram with an induced increase in membrane tension marked with a blue arrow. (E) Side views of tomograms without manipulation of membrane tension. (F) Changes in filament density for the tomograms shown in D and E. The blue arrow corresponds to 0 nm in the graph. All scale bars 200 nm. For details of methods, see Mueller *et al.*, 2017.

rate starts to decrease accordingly. The protrusion rate increases monotonically with N . At 50% of filament density, the protrusion rate is ~45% of the control value while the assembly rate changes by ~10% only. These results are closer to experimental observations than scenario 2.

With this, and together with the experimental observations discussed above, we stick to the intermediate scenario and form three subpopulations of filaments with different elongation rates to investigate the effect of removing formins distinguished by these properties. We know from knockout of both formins that this reduces filament density to about one-half. We do not know for sure whether the fraction of filaments vanishing upon knockout is the same as the fraction of filaments elongated by formins in control; we merely take it as the most reasonable assumption. Our population 1 is not elongated by formins but by another elongator, for example, Ena/VASP, and accounts for ~50% of filaments, $N_1 \sim N/2$. Population 2 is elongated by FMNL2, whereas population 3 is elongated by FMNL3 and comprises more filaments than 2, $N_3 \sim 1.7N_2$ (based on measured nucleation rates in vitro; Kage *et al.*, 2017). The formins' force-free polymerization rates ($V_P(f=0)$) have been chosen according to in vitro measurements (Kage *et al.*, 2017). We have set the polymerization rate of population 1 to the same value as in the simulations with one population. It is in between those of 2 and 3. The ratios among these three different elongation rates in vivo might be different from in vitro results. Therefore, we consider variations of them in the Supplemental Material (Supplemental Figures S5 and S6). Now with three subpopulations, each population has its own average length l_i and average force per filament f_i , such that the total force is $F = N_1f_1 + N_2f_2 + N_3f_3$, and $N = N_1 + N_2 + N_3$.

We decrease the area density starting from control in three different ways: by taking out populations 2 and 3 to mimic the formin knockout experiments, by taking out filaments from all three populations proportional to their fraction down to half of each (this case may also represent the Nap1-KO experiments), and by taking out population 1. We compare simulation results to the measured population mean value of a variety of experiments normalized to the control results of each type of experiment (Figure 6). We can see the robust monotonic relation between density and protrusion velocity regardless of the type of experiment. For the assembly rate, the fraction of the three populations matters to some degree. Reducing population 1 or all three populations proportionally leaves the assembly rate almost unchanged down to ~60% control density, and then causes a decrease by ~10–15%. Surprisingly, we see that if the slow and fast populations are taken out (knockout FMNL2/3 experiments) and population 1 remains, the assembly rate again stays almost unchanged as in the experimental results (Kage *et al.*, 2017).

These results also provide a qualitative explanation of individual formin knockdown experiments. Knocking down FMNL3 reduces the protrusion rate more than knocking down FMNL2 despite FMNL2 being the faster elongator (Block *et al.*, 2012; Kage *et al.*, 2017). FMNL3 contributes more to the filament density (Kage *et al.*, 2017) and thus also to the total force on the leading edge membrane and protrusion rate than FMNL2. The larger filament number compensates for the smaller force-free polymerization rate. We conclude that the differences in force-free polymerization rate between the three populations do not dominate the outcome of knockdown/knockout experiments because they are mitigated by the number ratios, force dependency of elongation, and the mechanical coupling by the leading edge membrane.

In the Supplemental Material, we further investigate how changes in the initial ratio of the filament populations affects the

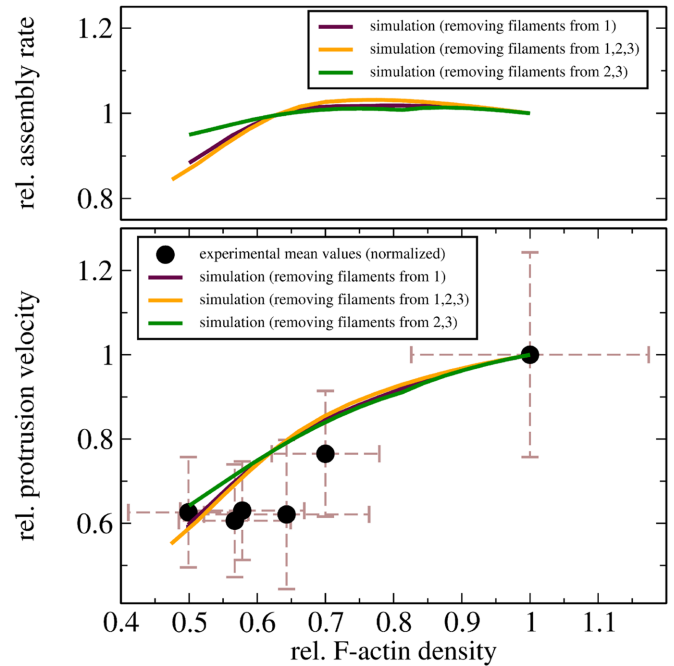


FIGURE 6: Experimental data points (normalized to their control measurements, mean with SD) and simulation results for the correlation between F-actin density, network assembly rate, and protrusion rate. We simulated three ways to decrease the number of filaments. Removing filaments from populations 2 and 3 mimics knockout of FMNL2/3. Removing filaments from all subpopulations to equal extents mimics knockout of Nap1. The assembly rate of the network changes very little (less than 5%) when we mimic the formin knockouts, and it changes ~10–15% when we take out filaments in other ways. The protrusion rate changes by ~40% in all cases. In the simulations, we use $N = 320$ filaments μm^{-1} with $N_1 = 160 \mu\text{m}^{-1}$, $N_2 = 60 \mu\text{m}^{-1}$, and $N_3 = 100 \mu\text{m}^{-1}$ for the control.

results (Supplemental Figure S7). If $N_2 < \sim 0.7 N_3$, then knocking down FMNL3 decreases the protrusion rate more than knocking down FMNL2, as also observed in experiments (Block *et al.*, 2012; Kage *et al.*, 2017).

Although major actin assemblies undergoing contraction in a myosin II-dependent manner are concentrated at cell flanks and lamellipodium rear of highly motile keratocytes (Svitkina *et al.*, 1997; Barnhart *et al.*, 2015), myosin II-mediated pulling is indirectly impacting on protrusion efficiency through contributing to lamellipodial rearward flow and to transition of filaments at the base of lamellipodia into lamella bundles (Medeiros *et al.*, 2006; Koestler *et al.*, 2008; Burnette *et al.*, 2011). We have thus also explored the effect of a constant contraction on the system. Such contraction events may even coincide with filament depolymerization (Zajac *et al.*, 2008; Reyman *et al.*, 2012; Fuhs *et al.*, 2014). However, the introduction of additional, active pulling forces did not significantly change the previously observed dependences of tension and flow velocity on N , and the principal, differential changes of protrusion and retrograde flow rates versus assembly rate (Supplemental Figure S8). The depth of the ER region in our model is coupled with the concentration of cross-linkers. In the Supplemental Material, we also investigate how changes in the total number of cross-linkers per cell may impact the depth of ER and the dynamics of the system (see Supplemental Material Section 5.3 and Supplemental Figure S9).

DISCUSSION

The mathematical model presented here offers a physical explanation for the conservation of network assembly rate and reduction in protrusion velocity and increase of the ratio R_F of force to filament number upon filament area density decrease. The model explains all previously and herein-described observations in terms of the properties of flow of a viscoelastic filament network with friction force against the cellular components stationary in the lab frame and the membrane, and a linear drag force resisting leading edge membrane motion. The assembly rate of the network can be maintained during decreasing protrusion, if retrograde flow speeds up. That speedup is caused in part by the decrease in friction (and viscosity). Retrograde flow also increases with decreasing area density due to a tension-based mechanism caused by lamellipodium height reduction. We found this mechanism to be essential for reproducing the experimental results by simulations, and this nicely correlates with network adaptations observed upon experimentally induced, transient changes of load exerted onto the tip membrane (Figure 4). Indeed, simulations showed that the tension-based mechanism alone would sufficiently explain experimental observations. However, we also included the effects of density-related elasticity, friction, and viscosity changes in our simulations, because it is reasonable to assume that they occur in our model cell system upon area density reduction.

In vitro, the force-free elongation rate of FMNL2 is faster than that of FMNL3 (Kage *et al.*, 2017), but knocking out FMNL3 entailed a larger drop in protrusion rate than knocking out FMNL2. FMNL3 is more actively nucleating filaments than FMNL2 (Kage *et al.*, 2017). Our modeling efforts suggest that the larger contribution of FMNL3 to filament density explains the stronger reduction of protrusion rate upon FMNL3 knockout compared with FMNL2 knockout in B16-F1 cells.

In Nap1 knockout experiments (generating cell populations with differential Hem1 expression), lamellipodial Arp2/3 activity is modulated. Even though we see the same correlation between F-actin area density and protrusion rate, we do not know at present whether actin network assembly rates are changed in this case. In fact, because Arp2/3 complex and cross-linker molecules mediate and maintain the structure of the network, it is tempting to speculate that in this case, network assembly rates will be affected. Indeed, Müller *et al.* (2017) clearly observed changes in growth rates of both individual filaments and protruding network. These changes depended on load and affected both network density and distribution of filament angles abutting the front, all of which could be explained by the geometry of Arp2/3-dependent branching (Mueller *et al.*, 2017). In contrast, only slight differences between angular distributions of filaments in control and FMNL2/3 knockouts could previously be found (Kage *et al.*, 2017). Modulation of Arp2/3 activity might thus affect angular distributions of filaments more severely, coinciding with changes in force transmission in the ER. Future experimental efforts will be aimed at clarifying these points.

The ER juxtaposed to the leading edge membrane does not play a central role for the mechanisms reported in this study as long as we consider steady motion. It relates the model network to actin-specific features like the F-actin bending modulus and the force dependency of polymerization (Gholami *et al.*, 2008), which may limit the maximum force that can be transmitted by the network (see also Supplemental Figures S1–S3). The ER mainly shapes the dynamics and explains characteristic properties of the force-velocity relation (Zimmermann *et al.*, 2012). Including it in our model allows for explaining both types of experiments (formin and Nap1 knockout and

force-velocity relation) with the same set of model assumptions, thus providing a unified picture.

Analysis of the force-velocity relation of lamellipodial motion (Prass *et al.*, 2006; Zimmermann *et al.*, 2010, 2012; Heinemann *et al.*, 2011) revealed that the force stalling protrusion is equal to the force required to drive retrograde flow with the network assembly rate. In line with these findings, our results suggest that protrusion forces at the leading edge are set by the properties of F-actin network flow in steady cell motion. The force driving retrograde flow is the force pushing the membrane. Adhesion force is transmitted only as friction force to the flow and leading edge and not by elastic elements fixed to adhesion sites. This mechanism agrees with the parameter dependence of force generation found in a variety of experiments (Prass *et al.*, 2006; Heinemann *et al.*, 2011; Zimmermann *et al.*, 2012; Kage *et al.*, 2017) and the results of this study.

MATERIALS AND METHODS

Generation of knockout cell lines using CRISPR/Cas9

B16-F1 mouse melanoma cells (ATCC CRL-6323) were grown in DMEM (4.5 g l⁻¹ glucose; Invitrogen, Germany) with 10% fetal calf serum (PAA Laboratories, Austria) and 2 mM glutamine (Thermo Fisher Scientific), and incubated at 37°C in the presence of 7.5% CO₂. For generating B16-F1 lines lacking the WRC subunit Nap1, CRISPR/Cas9-mediated gene disruption was performed as follows: a DNA target sequence corresponding to exon 1 of the murine *Nap1* gene was pasted into a CRISPR design tool (<http://tools.genome-engineering.org>). Resulting potential target sites with the highest efficiency scores were used for designing four distinct single guide RNA constructs (20 nucleotides) and tested for efficiency of down-regulating Nap1 expression in transient, bulk B16-F1 cell transfections. The most potent guide sequence mediating Nap1 gene disruption corresponded to 5'-GACGCCCGTGTCGTTGAGGA-3' (#4), and was ligated into expression plasmid pSpCas9(BB)-2A-Puro (Addgene plasmid ID:48139) using *BbsI* (Ran *et al.*, 2013). The resulting CRISPR/Cas9 plasmid was sequence-verified using primer 5'-GCACCGACTCGGTGCCAC-3'. For generation of stably disrupted, genome-edited cell lines, B16-F1 cells were transfected with a CRISPR/Cas9 plasmid variant conferring resistance to puromycin. Transfections were carried out on 10-cm dishes using 3 µg DNA in DMEM and 6 µl JetPrime reagent (Polyplus transfection) overnight. The next day, cells were transferred into medium containing 2.5 µg ml⁻¹ puromycin and selected for 4 d. To generate clones, cells were plated as single cell colonies, and cultured in conditioned medium until reaching a macroscopically visible size, followed by their transfer into individual dishes. Cell lysates were tested for Nap1 expression by Western blotting, and cells lacking apparent expression of Nap1 genotyped as follows: Upon expansion and growth to confluence in 6-cm dishes, cells were trypsinized, pelleted, and lysed adding 500 µl lysis buffer (100 mM Tris, pH 8.5, 5 mM EDTA, 0.2% SDS, 200 mM NaCl) containing 2.5 µl proteinase K (20 mg ml⁻¹). Samples were incubated overnight at 55°C. Nucleic acid extraction was performed by a standard phenol/chloroform precipitation procedure. Isolated genomic DNA was used as template in PCRs employing Phusion high-fidelity polymerase (New England Biolabs). Primers used for amplification of respective target gene loci were 5'-ATGTC-GCGCTCCGTGC-3' (fwd) and 5'-GATGTTGTAGAGGCGCGTGA-3' (rev). PCR products were examined on 2% agarose gels, excised from gels and purified with NucleoSpin Gel and PCR clean-up kit according to the manufacturer's instructions (Macherey-Nagel). DNA fragments were cloned into a zero blunt TOPO vector (Zero Blunt TOPO Cloning Kit for Sequencing; Invitrogen), as recommended by the manufacturer, and multiple, individually isolated alleles

sequenced for each cell line: In brief, single bacterial colonies were inoculated overnight and plasmid DNA purified using a NucleoSpin Plasmid kit (Macherey-Nagel), followed by target-site sequencing by MWG-Biotech (Ebersberg, Germany) using primer 5'-CAGGAAA-CAGCTATGAC-3'. Plasmid from individually purified bacterial colonies was examined for frameshift mutations such as deletions or insertions. Mutations generating stop codons shortly downstream from the target site were defined as "null" alleles. Cell lines exclusively harboring such alleles and thus lacking a detectable wild-type allele among ~20 individual sequencing reactions were selected for further analyses, and defined as Nap1 knockout (KO). Based on RNAi data in B16-F1 cells and genetic deletion of the hematopoietic Nap1 paralogue Hem1 in dendritic cells, Nap1-deficient B16-F1 cells were expected to be devoid of lamellipodia (Steffen *et al.*, 2004; Leithner *et al.*, 2016). Whereas most Nap1-deficient clones were strongly abrogated for lamellipodia formation, which could be equally rescued by enhanced green fluorescent protein (EGFP)-tagged Nap1 or EGFP-Hem1, selected, individual clones displayed lamellipodia to a variable extent, which depended on the extent of compensatory Hem1 expression and concomitant levels of the WRC subunit Scar/WAVE (Frieda Kage and Klemens Rottner, unpublished data). Albeit not reaching wild-type levels of Scar/WAVE and thus lamellipodia, two Nap1 null clones with low level Hem1 expression were selected for analyses of the consequences of differentially reduced Scar/WAVE gene dose on lamellipodial parameters: Arp2/3 complex incorporation, actin filament intensity, and protrusion rate, as well as cell migration.

F-actin and ArpC5A stainings and quantifications

For immunolabeling of the Arp2/3 complex component ArpC5A (formerly called p16A), cells were seeded onto glass coverslips coated with laminin (Sigma) diluted to 25 $\mu\text{g ml}^{-1}$ in 50 mM Tris (pH 7.4), 150 mM NaCl and incubated for 60 min. Cells were allowed to adhere overnight. Next, cells were fixed with prewarmed, 4% paraformaldehyde (PFA) in phosphate-buffered saline (PBS; pH 7.4) for 20 min and permeabilized with 0.05% Triton X-100 in PBS for 1 min. Cells were then blocked with 5% horse serum in 1% bovine serum albumin in PBS, and stained with monoclonal ArpC5A antibody (clone 323H3; undiluted hybridoma supernatant; Olazabal *et al.*, 2002), followed by Alexa Fluor 488-coupled secondary antibodies mixed with Alexa Fluor 594-coupled phalloidin (Invitrogen). For quantifying F-actin intensities, cells were treated as above except for fixing with a mixture of 4% PFA and 0.25% glutaraldehyde (GA) in PBS (pH 7.4), followed by permeabilization and staining with Alexa Fluor 488-labeled phalloidin. Images of fluorescently labeled cells were acquired as described (Steffen *et al.*, 2013) using 40 \times /1.3 numerical aperture (NA) Neofluar and 100 \times /1.4 NA Plan Apochromat oil objectives.

Fluorescence intensities of lamellipodial F-actin and Arp2/3 complex (ArpC5A) were determined by measuring average pixel intensities within lamellipodial regions and corrected for background essentially as described previously (Kage *et al.*, 2017), and as illustrated in Supplemental Figure S10. Fluorescence intensities in lamellipodial regions of Nap1 KO clones were compared with those of parental B16-F1 cells normalized to 1 (arbitrary units), and displayed as box-and-whiskers plots.

Video microscopy, determination of protrusion rates, and random migration speed

Live cell imaging of B16-F1 and Nap1 KO clones migrating on laminin (Sigma)-coated glass coverslips was done essentially as described (Kage *et al.*, 2017). In brief, cells were observed in open

heating chambers (Warner Instruments, Reading, UK) at 37°C and with microscopy medium (F12 HAM HEPES-buffered medium; Sigma) containing 10% fetal calf serum, 2 mM L-glutamine, and 1% penicillin/streptomycin. Phase-contrast, time-lapse images of protruding cells were routinely recorded over a time period of at least 5 min, acquiring an image every 5 s. Protrusion rates were determined based on kymographs generated by drawing lines from inside the cell and across the lamellipodium using MetaMorph software (Molecular Devices). Kymographs are space-time plots generated by pasting narrow cellular regions from each time point of a time-lapse series along the x-axis. Protrusion rates were determined by measuring the advancement of lamellipodia tips (y-axis) over time (x-axis). Three independent regions per cell were analyzed and averaged.

For random migration assays, cells were seeded subconfluently into laminin-coated, μ -slide four-well glass bottom microscopy chambers (Ibidi GmbH, Martinsried, Germany). After allowing cells to spread for at least 6 h, the chamber was mounted onto an inverted Axio observer equipped with a 37°C incubator, CO₂ atmosphere, and motorized, programmable microscopy stage (operated by Visiview software; Visitron GmbH, Puchheim, Germany). Phase-contrast movies were acquired on different, randomly chosen positions using a 10 \times /0.15NA Plan Neofluar objective for 10 h (frame rate: 6 h⁻¹). Randomly moving cells were manually tracked and migration speed determined using ImageJ software v1.46r (W. S. Rasband, ImageJ, U.S. National Institutes of Health, Bethesda, MD; <http://imagej.nih.gov/ij/>, 1997–2015).

3D-SIM

Before imaging, cells were prepared and stained for F-actin using phalloidin as described in *F-actin and ArpC5A stainings and quantifications*. Image panels shown in Supplemental Figure S4 were acquired on a Nikon SIM-E superresolution microscope equipped with a LU-N3-SIM 488/561/640 laser unit mounted on a Nikon Ti eclipse (Nikon). A piezo z-drive (Mad City Labs) was used to acquire three-dimensional (3D)-stacks composed of 20 slices using a step size of 0.05 μm (1 μm in total). Images were taken with a CFI Apochromat TIRF 100 \times /1.49 NA oil immersion objective (Nikon), a Hamamatsu Orca flash 4.0 LT camera, and an N-SIM motorized quad band filter combined with N-SIM 488 and 561 bandpass emission filters using laser line 488 driven by NIS-Elements software (Nikon). Reconstructions were carried out with the stack reconstruction tool (Nikon, NIS-Elements). Lamellipodium height was calculated according to the number of slices in which the lamellipodial network was clearly visible. Note that this method was employed to detect potential differences between KO and control cells, but cannot by any means report on real lamellipodial heights (known to be in the range of 100–200 nm (Small *et al.*, 2002), due to the shape of the point-spread function stretched in Z.

Proteomic analysis of B16-F1 cell lysates

Sample preparation for mass spectrometry. Protein pellets were resuspended in denaturation buffer (6 M urea, 2 M thiourea, 10 mM HEPES, pH 8.0), and into each sample UPS2 protein standard (Sigma-Aldrich) was added with a ratio of 1:3. Protein extracts were reduced with 12 mM dithiothreitol for 30 min at room temperature, followed by alkylation with 40 mM chloroacetamide for 20 min in the dark at room temperature. The endoproteinase LysC (Wako) was added following a protein:enzyme ratio of 50:1 and incubated for 4 h at room temperature. After dilution of the sample with four times digestion buffer (50 mM ammonium bicarbonate in water (pH 8.0), sequence grade-modified trypsin (Promega) was added (same protein:enzyme

ratio as for LysC) and digested overnight. Finally, trypsin and Lys-C activities were quenched by acidification of the reaction mixtures with trifluoroacetic acid to pH ~2. Afterward, peptides were extracted and desalted using StageTips (Rappsilber *et al.*, 2003).

LC-MS/MS analyses. For each injection, 1 µg peptides was separated on a monolithic column (100 µm i.d. × 2000 mm; MonoCap C18 High Resolution 2000 [GL Sciences] using 6 h gradient of increasing acetonitrile concentration at a flow rate of 300 nl/min). The Q Exactive Plus instrument (Thermo Fisher Scientific) was operated in the data-dependent mode with a full scan in the Orbitrap followed by top 10 MS/MS scans using higher-energy collision dissociation (HCD).

Data analyses. MaxQuant software, v1.5.2.8 (Cox and Mann, 2008) was used to identify and quantify proteins. The internal Andromeda search engine was used to search MS/MS spectra against a decoy mouse UniProt database (MOUSE.2014-10) containing forward and reverse sequences. The search included variable modifications of methionine oxidation and N-terminal acetylation, deamidation (NQ), and fixed modification of carbamidomethyl cysteine. Minimal peptide length was set to seven amino acids and the false discovery rate was set to 1% at both peptide and protein level. Unique and razor peptides were considered for quantification. The “match between runs” option and the iBAQ algorithm were enabled.

Copy number calculation. Lists of identified proteins were filtered to exclude reverse database hits, potential contaminants, and proteins only identified by site. Using the iBAQ intensity values, copy numbers were calculated as described in Schwanhäusser *et al.* (2011). Briefly, iBAQ intensities were log-transformed and plotted against known log-transformed absolute molar amounts of the spiked-in standard proteins (UPS2 standard). Linear regression was used to fit iBAQ intensities to absolute standard protein amounts. The slope and intercept from this calibration curve was then used to convert iBAQ intensities to molar amounts for all identified proteins. Cellular copy numbers were obtained by calculating the numbers of molecules using the Avogadro constant followed by division by the number of cells used in the experiment.

ACKNOWLEDGMENTS

This work has been supported by the Deutsche Forschungsgemeinschaft, grant Fa350/9-1 and a subproject of DFG Research Training Group GRK1558 (both to M.F.), as well as grant Ro2414/3-2 (to K.R.). We thank Brian Camley and Wouter-Jan Rappel for helpful discussions on the phase field method.

REFERENCES

Barnhart E, Lee KC, Allen GM, Theriot JA, Mogilner A (2015). Balance between cell-substrate adhesion and myosin contraction determines the frequency of motility initiation in fish keratocytes. *Proc Natl Acad Sci USA* 112, 5045–5050.

Barnhart EL, Lee KC, Keren K, Mogilner A, Theriot JA (2011). An adhesion-dependent switch between mechanisms that determine motile cell shape. *PLoS Biol* 9, e1001059.

Block J, Breitsprecher D, Kuhn S, Winterhoff M, Kage F, Geffers R, Duwe P, Rohn JL, Baum B, Brakebusch C, *et al.* (2012). FMNL2 drives actin-based protrusion and migration downstream of Cdc42. *Curr Biol* 22, 1005–1012.

Burnette DT, Manley S, Sengupta P, Sougrat R, Davidson MW, Kachar B, Lippincott-Schwartz J (2011). A role for actin arcs in the leading-edge advance of migrating cells. *Nat Cell Biol* 13, 371–381.

Camley BA, Zhao Y, Li B, Levine H, Rappel WJ (2013). Periodic migration in a physical model of cells on micropatterns. *Phys Rev Lett* 111, 158102.

Chen Z, Borek D, Padrick SB, Gomez TS, Metlagel Z, Ismail AM, Umetani J, Billadeau DD, Otwinowski Z, Rosen MK (2010). Structure and control of the actin regulatory WAVE complex. *Nature* 468, 533–538.

Courtemanche N, Lee JY, Pollard TD, Greene EC (2013). Tension modulates actin filament polymerization mediated by formin and profilin. *Proc Natl Acad Sci USA* 110, 9752–9757.

Cox J, Mann M (2008). MaxQuant enables high peptide identification rates, individualized p.p.b.-range mass accuracies and proteome-wide protein quantification. *Nat Biotechnol* 26, 1367–1372.

Danuser G, Allard J, Mogilner A (2013). Mathematical modeling of eukaryotic cell migration: insights beyond experiments. *Annu Rev Cell Dev Biol* 29, 501–528.

Delorme V, Machacek M, DerMardirossian C, Anderson KL, Wittmann T, Hanein D, Waterman-Storer C, Danuser G, Bokoch GM (2007). Cofilin activity downstream of Pak1 regulates cell protrusion efficiency by organizing lamellipodium and lamella actin networks. *Dev Cell* 13, 646–662.

Ehrlicher AJ, Krishnan R, Guo M, Bidan CM, Weitz DA, Pollak MR (2015). Alpha-actinin binding kinetics modulate cellular dynamics and force generation. *Proc Natl Acad Sci USA* 112, 6619–6624.

Falcke M (2016). Concentration profiles of actin-binding molecules in lamellipodia. *Physica D: Nonlinear Phenomena* 318–319, 50–57.

Fuhs T, Goegele M, Brunner CA, Wolgemuth CW, Kaes JA (2014). Causes of retrograde flow in fish keratocytes. *Cytoskeleton (Hoboken)* 71, 24–35.

Gardel ML, Shin JH, MacKintosh FC, Mahadevan L, Matsudaira P, Weitz DA (2004). Elastic behavior of cross-linked and bundled actin networks. *Science* 304, 1301–1305.

Gholami A, Falcke M, Frey E (2008). Velocity oscillations in actin-based motility. *New J Phys* 10, 033022.

Hansen SD, Mullins RD (2015). Lamellipodin promotes actin assembly by clustering Ena/VASP proteins and tethering them to actin filaments. *Elife* 4, e06585.

Heinemann F, Doschke H, Radmacher M (2011). Keratocyte lamellipodial protrusion is characterized by a concave force-velocity relation. *Biophys J* 100, 1420–1427.

Herant M, Dembo M (2010). Form and function in cell motility: from fibroblasts to keratocytes. *Biophys J* 98, 1408–1417.

Iwasa JH, Mullins RD (2007). Spatial and temporal relationships between actin-filament nucleation, capping, and disassembly. *Curr Biol* 17, 395–406.

Janmey PA, Hvidt S, Kas J, Lerche D, Maggs A, Sackmann E, Schliwa M, Stossel TP (1994). The mechanical properties of actin gels. Elastic modulus and filament motions. *J Biol Chem* 269, 32503–32513.

Jégou A, Carlier M-F, Romet-Lemonne G (2013). Formin mDia1 senses and generates mechanical forces on actin filaments. *Nat Commun* 4, 1883.

Ji L, Lim J, Danuser G (2008). Fluctuations of intracellular forces during cell protrusion. *Nat Cell Biol* 10, 1393–1400.

Joanny JF, Prost J (2009). Active gels as a description of the actin-myosin cytoskeleton. *HFSP J* 3, 94–104.

Kage F, Winterhoff M, Dimchev V, Mueller J, Thalheim T, Freise A, Bruhmann S, Kollasser J, Block J, Dimchev G, *et al.* (2017). FMNL formins boost lamellipodial force generation. *Nat Commun* 8, 14832.

Koestler SA, Auinger S, Vinzenz M, Rottner K, Small JV (2008). Differentially oriented populations of actin filaments generated in lamellipodia collaborate in pushing and pausing at the cell front. *Nat Cell Biol* 10, 306–313.

Koestler SA, Steffen A, Nemethova M, Winterhoff M, Luo N, Holleboom JM, Krupp J, Jacob S, Vinzenz M, Schur F, *et al.* (2013). Arp2/3 complex is essential for actin network treadmilling as well as for targeting of capping protein and cofilin. *Mol Biol Cell* 24, 2861–2875.

Kozlov MM, Bershadsky AD (2004). Processive capping by formin suggests a force-driven mechanism of actin polymerization. *J Cell Biol* 167, 1011–1017.

Krause M, Gautreau A (2014). Steering cell migration: lamellipodium dynamics and the regulation of directional persistence. *Nat Rev Mol Cell Biol* 15, 577–590.

Kroy K, Frey E (1996). Force-extension relation and plateau modulus for wormlike chains. *Phys Rev Lett* 77, 306–309.

Kruse K, Joanny JF, Julicher F, Prost J, Sekimoto K (2005). Generic theory of active polar gels: a paradigm for cytoskeletal dynamics. *Eur Phys J E Soft Matter* 16, 5–16.

Kruse K, Joanny JF, Julicher F, Prost J (2006). Contractility and retrograde flow in lamellipodium motion. *Phys Biol* 3, 130–137.

Kunda P, Craig G, Dominguez V, Baum B (2003). Abi, Sra1, and Kette control the stability and localization of SCAR/WAVE to regulate the formation of actin-based protrusions. *Curr Biol* 13, 1867–1875.

Lai FP, Szczodrak M, Block J, Faix J, Breitsprecher D, Mannherz HG, Stradal TE, Dunn GA, Small JV, Rottner K (2008). Arp2/3 complex

- interactions and actin network turnover in lamellipodia. *EMBO J* 27, 982–992.
- Leithner A, Eichner A, Muller J, Reversat A, Brown M, Schwarz J, Merrin J, de Gorter DJ, Schur F, Bayerl J, et al. (2016). Diversified actin protrusions promote environmental exploration but are dispensable for locomotion of leukocytes. *Nat Cell Biol* 18, 1253–1259.
- Machesky LM, Insall RH (1998). Scar1 and the related Wiskott-Aldrich syndrome protein, WASP, regulate the actin cytoskeleton through the Arp2/3 complex. *Curr Biol* 8, 1347–1356.
- MacKintosh FC, Kas J, Janmey PA (1995). Elasticity of semiflexible biopolymer networks. *Phys Rev Lett* 75, 4425–4428.
- Medeiros NA, Burnette DT, Forscher P (2006). Myosin II functions in actin-bundle turnover in neuronal growth cones. *Nat Cell Biol* 8, 215–226.
- Mejillano MR, Kojima S, Applewhite DA, Gertler FB, Svitkina TM, Borisy GG (2004). Lamellipodial versus filopodial mode of the actin nanomachinery: pivotal role of the filament barbed end. *Cell* 118, 363–373.
- Mogilner A, Oster G (2003). Force generation by actin polymerization II: the elastic ratchet and tethered filaments. *Biophys J* 84, 1591–1605.
- Mueller J, Szep G, Nemethova M, de Vries I, Lieber AD, Winkler C, Kruse K, Small JV, Schmeiser C, Keren K, et al. (2017). Load adaptation of lamellipodial actin networks. *Cell* 171, 188–200 e116.
- Mullins RD, Heuser JA, Pollard TD (1998). The interaction of Arp2/3 complex with actin: nucleation, high affinity pointed end capping, and formation of branching networks of filaments. *Proc Natl Acad Sci USA* 95, 6181–6186.
- Nakamura F, Osborn E, Janmey PA, Stossel TP (2002). Comparison of filamin A-induced cross-linking and Arp2/3 complex-mediated branching on the mechanics of actin filaments. *J Biol Chem* 277, 9148–9154.
- Nickaen M, Novak IL, Pulford S, Rumack A, Brandon J, Slepchenko BM, Mogilner A (2017). A free-boundary model of a motile cell explains turning behavior. *PLoS Comput Biol* 13, e1005862.
- Olazabal IM, Caron E, May RC, Schilling K, Knecht DA, Machesky LM (2002). Rho-kinase and myosin-II control phagocytic cup formation during CR, but not FcγR, phagocytosis. *Curr Biol* 12, 1413–1418.
- Pollard TD, Borisy GG (2003). Cellular motility driven by assembly and disassembly of actin filaments. *Cell* 112, 453–465.
- Pollard TD, Cooper JA (2009). Actin, a central player in cell shape and movement. *Science* 326, 1208–1212.
- Ponti A, Machacek M, Gupton SL, Waterman-Storer CM, Danuser G (2004). Two distinct actin networks drive the protrusion of migrating cells. *Science* 305, 1782–1786.
- Ponti A, Matov A, Adams M, Gupton S, Waterman-Storer CM, Danuser G (2005). Periodic patterns of actin turnover in lamellipodia and lamellae of migrating epithelial cells analyzed by quantitative fluorescent speckle microscopy. *Biophys J* 89, 3456–3469.
- Prass M, Jacobson K, Mogilner A, Radmacher M (2006). Direct measurement of the lamellipodial protrusive force in a migrating cell. *J Cell Biol* 174, 767–772.
- Ran FA, Hsu PD, Wright J, Agarwala V, Scott DA, Zhang F (2013). Genome engineering using the CRISPR-Cas9 system. *Nat Protoc* 8, 2281–2308.
- Rappilber J, Ishihama Y, Mann M (2003). Stop and go extraction tips for matrix-assisted laser desorption/ionization, nanoelectrospray, and LC/MS sample pretreatment in proteomics. *Anal Chem* 75, 663–670.
- Razbin M, Falcke M, Benetatos P, Zippelius A (2015). Mechanical properties of branched actin filaments. *Phys Biol* 12, 046007.
- Reymann AC, Boujemaa-Paterski R, Martiel JL, Guerin C, Cao W, Chin HF, De La Cruz EM, Thery M, Blanchoin L (2012). Actin network architecture can determine myosin motor activity. *Science* 336, 1310–1314.
- Rottner K, Faix J, Bogdan S, Linder S, Kerkhoff E (2017). Actin assembly mechanisms at a glance. *J Cell Sci* 130, 3427–3435.
- Rottner K, Hall A, Small JV (1999). Interplay between Rac and Rho in the control of substrate contact dynamics. *Curr Biol* 9, 640–648.
- Schermelleh L, Heintzmann R, Leonhardt H (2010). A guide to super-resolution fluorescence microscopy. *J Cell Biol* 190, 165–175.
- Schwahnhauser B, Busse D, Li N, Dittmar G, Schuchhardt J, Wolf J, Chen W, Selbach M (2011). Global quantification of mammalian gene expression control. *Nature* 473, 337–342.
- Shao D, Rappel WJ, Levine H (2010). Computational model for cell morphodynamics. *Phys Rev Lett* 105, 108104.
- Shekhar S, Pernier J, Carlier MF (2016). Regulators of actin filament barbed ends at a glance. *J Cell Sci* 129, 1085–1091.
- Shemesh T, Bershadsky AD, Kozlov MM (2012). Physical model for self-organization of actin cytoskeleton and adhesion complexes at the cell front. *Biophys J* 102, 1746–1756.
- Shemesh T, Kozlov MM (2007). Actin polymerization upon processive capping by formin: a model for slowing and acceleration. *Biophys J* 92, 1512–1521.
- Shemesh T, Verkhovsky AB, Svitkina TM, Bershadsky AD, Kozlov MM (2009). Role of focal adhesions and mechanical stresses in the formation and progression of the lamellipodium-lamellum interface [corrected]. *Biophys J* 97, 1254–1264.
- Small JV, Resch GP (2005). The comings and goings of actin: coupling protrusion and retraction in cell motility. *Curr Opin Cell Biol* 17, 517–523.
- Small JV, Stradal T, Vignal E, Rottner K (2002). The lamellipodium: where motility begins. *Trends Cell Biol* 12, 112–120.
- Steffen A, Ladwein M, Dimchev GA, Hein A, Schwenkmezger L, Arens S, Ladwein KI, Margit Holleboom J, Schur F, Victor Small J, et al. (2013). Rac function is crucial for cell migration but is not required for spreading and focal adhesion formation. *J Cell Sci* 126, 4572–4588.
- Steffen A, Rottner K, Ehinger J, Innocenti M, Scita G, Wehland J, Stradal TE (2004). Sra-1 and Nap1 link Rac to actin assembly driving lamellipodia formation. *EMBO J* 23, 749–759.
- Suraneni P, Rubinstein B, Unruh JR, Durnin M, Hanein D, Li R (2012). The Arp2/3 complex is required for lamellipodia extension and directional fibroblast cell migration. *J Cell Biol* 197, 239–251.
- Svitkina TM, Borisy GG (1999). Arp2/3 complex and actin depolymerizing factor/cofilin in dendritic organization and treadmill of actin filament array in lamellipodia. *J Cell Biol* 145, 1009–1026.
- Svitkina TM, Bulanova EA, Chaga OY, Vignjevic DM, Kojima S, Vasiliev JM, Borisy GG (2003). Mechanism of filopodia initiation by reorganization of a dendritic network. *J Cell Biol* 160, 409–421.
- Svitkina TM, Verkhovsky AB, McQuade KM, Borisy GG (1997). Analysis of the actin-myosin II system in fish epidermal keratocytes: mechanism of cell body translocation. *J Cell Biol* 139, 397–415.
- Wu C, Asokan SB, Berginski ME, Haynes EM, Sharpless NE, Griffith JD, Gomez SM, Bear JE (2012). Arp2/3 is critical for lamellipodia and response to extracellular matrix cues but is dispensable for chemotaxis. *Cell* 148, 973–987.
- Zajac M, Dacanay B, Mohler WA, Wolgemuth CW (2008). Depolymerization-driven flow in nematode spermatozoa relates crawling speed to size and shape. *Biophys J* 94, 3810–3823.
- Zimmermann J, Brunner C, Enculescu M, Goegler M, Ehrlicher A, Kas J, Falcke M (2012). Actin filament elasticity and retrograde flow shape the force-velocity relation of motile cells. *Biophys J* 102, 287–295.
- Zimmermann J, Enculescu M, Falcke M (2010). Leading-edge-gel coupling in lamellipodium motion. *Phys Rev E* 82, 051925.